Ultrasonics Sonochemistry 82 (2022) 105896

Contents lists available at ScienceDirect

Ultrasonics Sonochemistry

journal homepage: www.elsevier.com/locate/ultson

Ultrasound-assisted facile one-pot synthesis of ternary MWCNT/MnO_2/rGO nanocomposite for high performance supercapacitors with commercial-level mass loadings

Bhaskar J. Choudhury [a], Vijayanand S. Moholkar [a,b,*]

[a] School of Energy Science and Engineering, Indian Institute of Technology Guwahati, Guwahati 781 039, Assam, India
[b] Department of Chemical Engineering, Indian Institute of Technology Guwahati, Guwahati 781 039, Assam, India

ARTICLE INFO

Keywords:
Supercapacitors
Ultrasound
Energy density
Graphene
Carbon nanotubes
Manganese oxide

ABSTRACT

Commercial application of supercapacitors (SCs) requires high mass loading electrodes simultaneously with high energy density and long cycle life. Herein, we have reported a ternary multi-walled carbon nanotube (MWCNT)/MnO_2/reduced graphene oxide (rGO) nanocomposite for SCs with commercial-level mass loadings. The ternary nanocomposite was synthesized using a facile ultrasound-assisted one-pot method. The symmetric SC fabricated with ternary MWCNT/MnO_2/rGO nanocomposite demonstrated marked enhancement in capacitive performance as compared to those with binary nanocomposites (MnO_2/rGO and MnO_2/MWCNT). The synergistic effect from simultaneous growth of MnO_2 on the graphene and MWCNTs under ultrasonic irradiation resulted in the formation of a porous ternary structure with efficient ion diffusion channels and high electrochemically active surface area. The symmetric SC with commercial-level mass loading electrodes (~12 mg cm^{-2}) offered a high specific capacitance (314.6 F g^{-1}) and energy density (21.1 W h kg^{-1} at 150 W kg^{-1}) at a wide operating voltage of 1.5 V. Moreover, the SC exhibits no loss of capacitance after 5000 charge–discharge cycles showcasing excellent cycle life.

1. Introduction

In the quest for the development of reliable and efficient energy storage systems, supercapacitors (SCs) have received considerable attention [1]. Carbon–based materials have been extensively studied for electric double–layer capacitors (EDLCs), where the charge storage takes place via charge separation at the electrode–electrolyte interface [2,3]. Carbon-based EDLC materials, viz. activated carbon, graphene, carbon nanotubes (CNTs), exhibit high power densities and ultra-long cycle life but deliver low energy densities. On the other hand, the transition metal oxides/hydroxides and conducting polymers are being explored as pseudocapacitors (PCs) where the charge storage is based on the quick and reversible surface redox reactions [4]. The PCs can deliver high capacitance and energy density via the surface Faradaic reactions but shows relatively poor cycle stability. Therefore, hybrid composites combining both EDLC and pseudocapacitive materials are viable options for high-performance SCs.

The previous literature has demonstrated the potential of manganese dioxide (MnO_2) as a pseudocapacitive material [5-8]. Binary nanocomposites of MnO_2 with various conductive materials viz. MnO_2/activated carbon [9], MnO_2/graphene [10,11], MnO_2/conducting polymers [12], MnO_2/CNT [13,14] have been synthesized to obtain enhanced electrochemical properties. The nanocomposites of graphene/CNTs and MnO_2 have proven their effectiveness to overcome the difficulties of poor electrical conductivity, cycle stability of pristine MnO_2, and the low energy density of carbon components via synergistic effects. The undesired restacking graphene layers due to their π–π interaction and van der Waals forces leads to a substantial reduction in the active surface area of graphene-based electrodes [15,16]. Consequently, relatively poor capacitive performance is obtained for the graphene-based SCs due to hindered charge transport. The addition of various nanomaterials such as 1-D CNTs, metal oxide nanoparticles, and polymers in the graphene framework could work as spacers to prevent the restacking of graphene sheets and graphene-based nanocomposites with superior capacitive performance could be obtained [16,17].

The binary nanocomposites of MnO_2 with graphene or CNTs for SC applications have been well reported in the existing literature [11,18-25]. On the other hand, literature on SCs based on ternary

* Corresponding author at: School of Energy Science and Engineering, Indian Institute of Technology Guwahati, Guwahati 781 039, Assam, India.
E-mail address: vmoholkar@iitg.ac.in (V.S. Moholkar).

https://doi.org/10.1016/j.ultsonch.2021.105896
Received 26 November 2021; Received in revised form 16 December 2021; Accepted 24 December 2021
Available online 27 December 2021

nanocomposites of graphene, CNTs, and MnO_2 are relatively small. The previous literature [20,26-29] on ternary composites showed superior electrochemical performance as compared to binary nanocomposite as SC electrodes. Lei *et al.* [26] synthesized a ternary nanocomposite by intercalating graphene sheets via MnO_2-CNTs functionalized with poly (diallyldimethylammonium chloride) *via* a multistep process and demonstrated enhanced capacitive properties. Cheng et al. used a sonochemical approach to prepare rGO/MnO_2 composite and later added functionalized few-walled CNTs (fFWNTs) to fabricate graphene/MnO_2/fFWNTs films through a vacuum filtration method [27]. Jin *et al.* electrodeposited MnO_2 on a CNT buckypaper paper and then soaked as prepared MnO_2/CNT paper on graphene dispersion for adsorption rGO on its surface [20]. In another study, Zhu *et al.* synthesized 3D CNT–graphene–Ni hybrids through a two-step chemical vapor deposition (CVD) process and later used poly ethylene glycol (PEG) based reduction of $KMnO_4$ to obtain 3D MnO_2–CNT–graphene–Ni hybrids [28]. Similarly, Jiang *et al.* first synthesized rGO/CNTs-Ni composite via an annealing and CVD based process followed by a hydrothermal method to deposit MnO_2 on the surface of rGO/CNTs-Ni [29]. The synthesis methods presented in these previous studies were either multi-step or often involve complex procedures and high temperatures. Therefore, a simple and fast synthesis process for the ternary composites is very essential.

The MnO_2/carbon–based nanocomposites reported in the literature have demonstrated remarkable enhancement in capacitance, cycle stability, and rate capability [9,11,13,14,30]. However, most of these studies were performed at very low electrode mass loadings (~1 – 2 mg cm^{-2}). In low mass loading electrodes, the actual amount of energy stored is very low, thereby limiting their practical application in energy storage devices [31]. Usually, for practical/commercial applications the mass loading of the electrodes should be $\geq$ 10 mg cm^{-2} [32-34]. A substantial reduction in the capacitance and energy density is observed for the commercial level electrode mass loading, particularly at high current densities. This is a collective consequence of blocked ion transportation pathways, poor electrolyte accessibility, poor wetting of electrodes, increased electrical resistance, and ultra–long ion transport channels [32,35]. Therefore, achieving high energy density simultaneously with high power density is a challenge in the fabrication of SC electrodes with commercial level mass loadings.

Herein, we have reported a "one-pot" ultrasound-assisted synthesis of MnO_2 decorated rGO/MWCNT based ternary nanocomposite for SCs. The ternary MWCNT/MnO_2/rGO (MnGC) nanocomposite possessed a mesoporous structure with abundant ion diffusion channels together with a high electrochemically active surface area. When SCs were assembled using MnGC as electrodes, the device exhibited a high cell voltage of 1.5 V in a 1 M Na_2SO_4 electrolyte. Moreover, the device demonstrated superb gravimetric capacitance, high energy density, and excellent cycle stability with no loss of capacitance after 5000 charge–discharge cycles. It is noteworthy that the high supercapacitive performances of the devices were obtained at commercial-level electrode mass loadings (~12 mg cm^{-2}). The capacitance and energy density of the ternary MnGC based SC was substantially higher than those of the SCs with binary MnC (MnO_2/MWCNTs) and MnG (MnO_2/rGO) composites synthesized by us.

2. Experimental section

2.1. Synthesis of ternary MWCNT/MnO_2/rGO nanocomposite

Graphene oxide was prepared using a modified Hummers method and subsequently reduced using hydrazine to obtain reduced graphene oxide (rGO) as reported in our previous study [36]. The multi-walled carbon nanotubes (MWCNTs, Reinste Nano Ventures Ltd., India) were purified and functionalized with nitric acid to improve their dispersion (please refer to the Supplementary material).

The prepared rGO and MWCNTs were added to 200 mL ultrapure water (rGO:MWCNTs = 8:2 ratio) and vigorously sonicated (100 W, 37 kHz) for 30 min to exfoliate the rGO and to obtain a homogeneous dispersion (3 mg mL^{-1}) of rGO/MWCNTs. Then, $MnSO_4{\cdot}H_2O$ (3 mmol) was added to the above dispersion under sonication. An aqueous solution of $KMnO_4$ (80 mL, 0.025 M) was added drop-wise to the reaction mixture under continuous sonication. The reaction mixture was further sonicated for another 30 min and then allowed to settle. The settled precipitate was filtered, washed with excess water, and oven-dried at 70 °C to obtain the MWCNT/MnO_2/rGO (MnGC) nanocomposite.

For comparison, binary nanocomposites, MnO_2/MWCNT (MnC) and MnO_2/rGO (MnG), were also synthesized. In this case, either MWCNTs or rGO was dispersed in 200 mL ultrapure water using sonication and further, the same synthesis procedure as used in MnGC nanocomposite was followed.

2.2. Materials characterization

The synthesized materials were characterized using X-ray diffraction (XRD), Raman spectroscopy, field emission scanning electron microscope (FESEM), transmission electron microscope (TEM), energy-dispersive spectroscopy (EDS), and Brunauer-Emmett-Teller (BET) surface area analysis. The details of characterization and the analysis are provided in the Supplementary material.

2.3. Electrochemical measurements

The working electrodes were prepared by mixing electro-active material (80 wt%), carbon black (10 wt%), and PTFE (10 wt%) in ethanol; and coating on stainless steel current collectors. The electrodes were dried overnight at 80 °C. The disc electrodes (dia. ~ 1.5 cm) had a mass loading of ~ 12 mg cm^{-2} of active materials. The electrochemical tests were performed in a two-electrode configuration using a split type coin cell (MTI Corporation, USA) assembly. Two-electrode symmetric cells were constructed with two similar electrodes, a cellulose separator and Na_2SO_4 (300 μL) as the electrolyte. Electrochemical tests were performed with a multi-channel M204 Potentiostat/Galvanostat (Metrohm Autolab). Cyclic voltammetry (CV), galvanostatic charge–discharge analyses (GCD), and electrochemical impedance spectroscopy (EIS) were used to determine the various performance parameters of the assembled SC devices.

The specific capacitances of the composite SC electrodes (based on two-electrode symmetric cell), as well as the energy and power densities of the SC devices, were calculated using the procedure described in the Supplementary material.

3. Results and discussion

3.1. Materials characterization

The MnO_2 nanoparticles were grown on the surface of MWCNTs and rGO via an ultrasound–assisted redox reaction. The growth of MnO_2 nanostructures on the carbon substrates (viz. MWCNTs and rGO) was achieved through the formation of Mn^{4+} as a result of oxidation/reduction reaction between Mn^{2+} and Mn^{7+} ions [37]. The loading MnO_2 on the synthesized nanocomposites i.e. MnC, MnG, and MnGC were ~ 37 – 39 wt%. The MnO_2 content was calculated from the weight difference before and after the growth of MnO_2 on the rGO/MWCNTs. Moreover, we also calculated the MnO_2 content by dissolving the composite in 1 M HCl solution followed by filtering and weighing the undissolved rGO/MWCNTs as reported in the literature [18] and obtained similar results. Fig. 1 represents the process of MnGC nanocomposite synthesis and the schematic illustration of the experimental setup used for the synthesis is shown in Fig. S1 (in Supplementary material).

The X–ray diffraction patterns were recorded over the range of 2θ = 10 – 70° (at a scan rate of 5° min^{-1}) and shown in Fig. 2a. MWCNTs exhibited a high–intensity characteristic peak at 2θ = 26° and a smaller

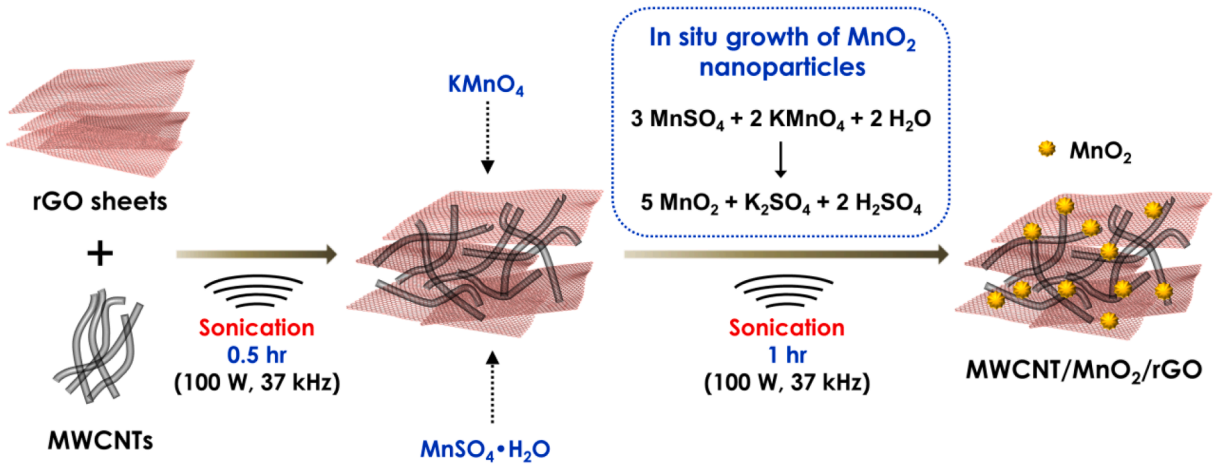

Fig. 1. Schematic illustration of "one-pot" ultrasound-assisted synthesis of the MWCNT/MnO_2/rGO nanocomposite.

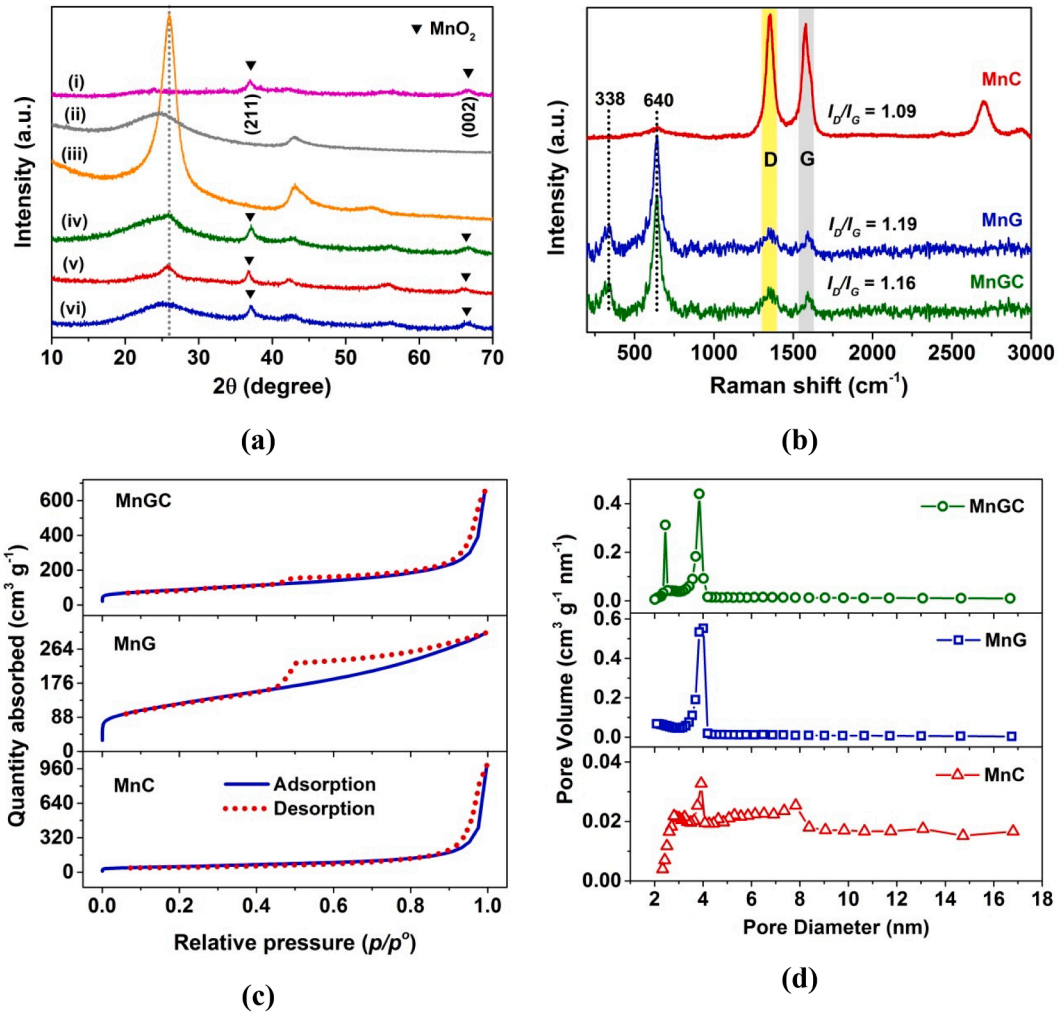

Fig. 2. (a) XRD patterns of (i) MnO_2, (ii) rGO, (iii), MWCNT, (iv) MnGC, (v) MnC, (vi) MnG; (b) Raman spectra, (c) nitrogen adsorption–desorption isotherms, and (d) pore size distribution of MnC, MnG, and MnGC nanocomposites.

peak at $2\theta = 43^\circ$ conforming to (0 0 2) and (1 0 0) graphitic carbon peaks, respectively. Similarly, the pristine reduced graphene oxide also showed the (0 0 2) and (1 0 0) peaks at $2\theta = 24.8^\circ$ and 43°. The diffraction peak corresponding to (0 0 2) plane of the rGO was broader, whereas it was sharper in the case of MWCNTs supporting the higher crystallinity of the carbon nanotubes. The XRD patterns of binary nanocomposites, MnC and MnG prominently showed the (0 0 2) peaks of both MWCNT and rGO, respectively. The MnGC nanocomposite showed a combination of broader and an adjacent sharper peak ascertaining the (0 0 2) planes of both rGO and MWCNT. The intensity of (0 0 2) plane at $2\theta = 26^\circ$ was

reduced in the composites due to the growth of MnO_2 on the surface of MWCNTs/rGO. Moreover, the intensity of the (1 0 0) plane was also low in the nanocomposites. The presence of two small and broad peaks at $2\theta = 37^\circ$ and 66.3° could be related to the (2 1 1) and (0 0 2) planes of MnO_2, respectively. The XRD patterns of the pristine MnO_2 (synthesized via the same method without any carbon substrates) were also compared with the XRD patterns of the composite, and two similar peaks were observed at $2\theta = 37^\circ$ and 66.3° corresponding to (2 1 1) and (0 0 2) planes of poorly crystalline MnO_2.[37] Thus, the XRD results confirmed the existence of MnO_2 in the nanocomposite. The weak intensity of MnO_2 referred to its poor crystallinity, which could be due to the small size of MnO_2 particles [13]. Additionally, amorphous manganese oxides are expected to have higher capacitance than their crystalline counterparts due to shorter length of diffusion and high ionic conductivity [14].

The structural features and composition of the nanomaterials were further characterized using the Raman spectroscopy technique. Raman spectra of MWCNTs and rGO (Fig. S2 in Supplementary material) exhibited two distinct D and G bands. The G band characterizes the vibrational mode of sp^2 hybridized carbon atoms whereas the D band signifies defects present in the sp^2 carbon rings. The bands of MWCNTs were sharp and observed at 1350 (D band) and 1574 (G band) cm^{-1}, respectively. The rGO exhibited relatively broader peaks at 1352 cm^{-1} (D band) and 1598 cm^{-1} (G band). The intensity ratio of D and G bands (I_D/I_G) corresponds to the degree of disorder present in the carbon frameworks. The I_D/I_G values for the MWCNTs and rGO were 1.05 and 1.18, respectively; indicating the higher degree of structural defects present in rGO which were introduced during the hydrazine reduction process. The D and G bands were present in the Raman spectra of all the nanocomposites and the I_D/I_G ratios were 1.09 (MnC), 1.19 (MnG), and 1.16 (MnGC), respectively (Fig. 2b). A prominent peak at $\sim$ 640 cm^{-1} was observed for all the nanocomposites which could be attributed to the Mn–O vibration in MnO_2. Whereas another weak peak at $\sim$ 338 cm^{-1} originating from O–Mn–O vibration mode is also observed in the Raman spectra of MnG and MnGC [10,14,38]. The presence of Mn–O, and O–Mn–O vibration modes supported the XRD results and thus confirmed the presence of MnO_2 in the nanocomposite.

The BET measurements were performed to find the specific surface area and pore size of the synthesized samples. Fig. 2c shows the N_2 adsorption–desorption isotherms of the nanocomposites. A surface area of $\sim$ 434 $m^2\ g^{-1}$ was obtained for MnG, as compared to $\sim$ 189 $m^2\ g^{-1}$ of MnC and $\sim$ 313 $m^2\ g^{-1}$ of MnGC. The adsorption–desorption isotherms of all the three nanocomposites were observed to be type IV isotherms with hysteresis loops due to capillary condensation in the mesopores after monolayer–multilayer adsorption. The H1 type hysteresis loop observed for MnC sample could be attributed to the presence of cylindrical pores with facile pore connectivity. The MnG sample showed an H2 type of hysteresis loop possibly due to the presence of uniform channel–like networks of mesopores with narrow openings. Interestingly, the hysteresis loop of the MnGC could be correlated to both H1 and H2 type hysteresis loops. The influence of H1 and H2 type loops is essentially due to the presence of both cylindrical pores and narrow channel–like mesoporous channels. The respective surface areas of MWCNTs and MnO_2 were $\sim$ 252 and 175 $m^2\ g^{-1}$, respectively. The surface area of pristine rGO was $\sim$ 555 $m^2\ g^{-1}$ as reported in our previous study [36]. Adsorption–desorption isotherms of MWCNTs and MnO_2 (Fig. S3a, b in Supplementary material) were found to be type IV isotherms with H1 and H2 type of hysteresis loops, respectively. The H2 type hysteresis loop of MnO_2 indicated the presence of narrow slit–like pores with irregularly shaped voids. The Barrett–Joyner–Halenda (BJH) model was used to obtain the pore–size distributions (shown in Fig. 2d and Fig. S3c, d in Supplementary material) of the synthesized nanomaterials. The nanocomposites along with the pristine MWCNTs and MnO_2 demonstrated mesoporous distribution in the range 2 – 18 nm range. The average pore diameters of the MnO_2, MWCNTs, MnC, MnG, and MnGC were found to be 4.40, 6.32, 7.42, 4.05, and 4.59 nm, respectively. The narrow pore size distribution of the samples is beneficial for better transport of electrolyte ions. Several studies have revealed that mesopore networks in the range of 2 – 5 nm could provide efficient pathways for easier ion diffusion to the core of electrodes [39,40]. Improved and faster ion transport essentially augments the capacitive performance of the electrode material. Moreover, the high pore volumes of nanocomposites (Table S1 in Supplementary material) could be expected to provide abundant active sites for surface redox reactions and double–layer formation.

The morphologies of the synthesized nanomaterials were studied using FE–SEM and TEM images. The MWCNTs had tubular structures with an outer diameter of 5 – 30 nm and a smooth surface (Fig. S4a–b in Supplementary material). Fig. S4c–d (in Supplementary material) revealed the crumpled sheet–like morphology of synthesized rGO. The FE–SEM and TEM images (Fig. S4e–f in Supplementary material) indicated that the MnO_2 nanoparticles were aggregate of grain–like structures making it look like a spiked MnO_2 sphere. These nanograins have varying diameters (10–30 nm) and lengths varying from 60 nm to sometimes more than 100 nm. The FE–SEM images of the nanocomposites (in Fig. 3) clearly showed the presence of MnO_2 in the carbon substrates.

The morphologies of the MnO_2 in the MnG were similar to the pristine MnO_2 with densely aggregated grains on the rGO surface. Whereas in the MnC composite the loosely aggregated grains of MnO_2 were observed on the surface of MWCNTs which could be due to the relatively lesser packing density of the MWCNTs as compared to rGO. In the MnGC nanocomposite, the MnO_2 grains were efficiently grown on the surface of both rGO and MWCNTs with relatively lesser aggregation than MnG nanocomposite. The TEM images of the nanocomposites (Fig. 4a-c) showed that MnO_2 particles were grown on the external surface of the MWCNTs and rGO in the nanocomposites. The relatively dense distribution of MnO_2 in MnG as compared to MnGC and MnC nanocomposites was also evident from the TEM images, thus supporting the FE–SEM results. The growth of MnO_2 on the carbon substrates (viz. MWCNTs and rGO) could form hierarchal mesoporous networks. As a result, the electroactive surface area available for electrolyte ions would increase and facilitate EDL formation and surface redox reactions. The elemental mappings and EDX spectra of the MnGC, MnC, and MnG nanocomposites are shown in Fig. 4d, Fig. S5a-b, and Fig. S6a-c (in Supplementary material), which also confirmed the presence of Mn, C, and O elements in the nanocomposites.

3.2. Electrochemical performance

To study the electrochemical performance of the nanocomposites, symmetric SCs were fabricated using two identical electrodes, a cellulose separator soaked in 1 M Na_2SO_4 electrolyte (cell assembly is shown in Fig. 5). The mass loading of each electrode was $\sim$ 12 mg cm^{-2}. In symmetric SCs, the charge stored in the positive and the negative electrodes are similar and therefore the potential window of the device is limited by the dissociation of the electrolyte. Typically, the potential window of common acidic and basic aqueous electrolytes is limited to 1 V due to O_2 and H_2 gas evolution from the electrolysis of water. Conversely, in neutral aqueous electrolytes such as Na_2SO_4, higher working potentials could be achieved as the low concentration of H^+ and OH^- ions delays the gas evolution reactions [41,42]. In our study, we were able to obtain a wide potential window of 1.5 V in 1 M Na_2SO_4 for the symmetric SCs (please refer to Fig. S7 in Supplementary material). This wide potential window is relatively higher as compared to other similar studies in the existing literature (please refer to Table S2, and 3 in Supplementary material).

The assembled SC cells were subjected to cyclic voltammetry (CV) tests at scan rates of 5 – 50 mV s^{-1}. The CV curves of the pristine MWCNTs, rGO, MnC, MnG, and MnGC at a scan rate of 10 mV s^{-1} are shown in Fig. 6a. It is observed that the CV curves of the nanocomposites are quasi–rectangular, indicating superior capacitive behavior of the nanocomposites [43]. There is a presence of very weak redox behavior

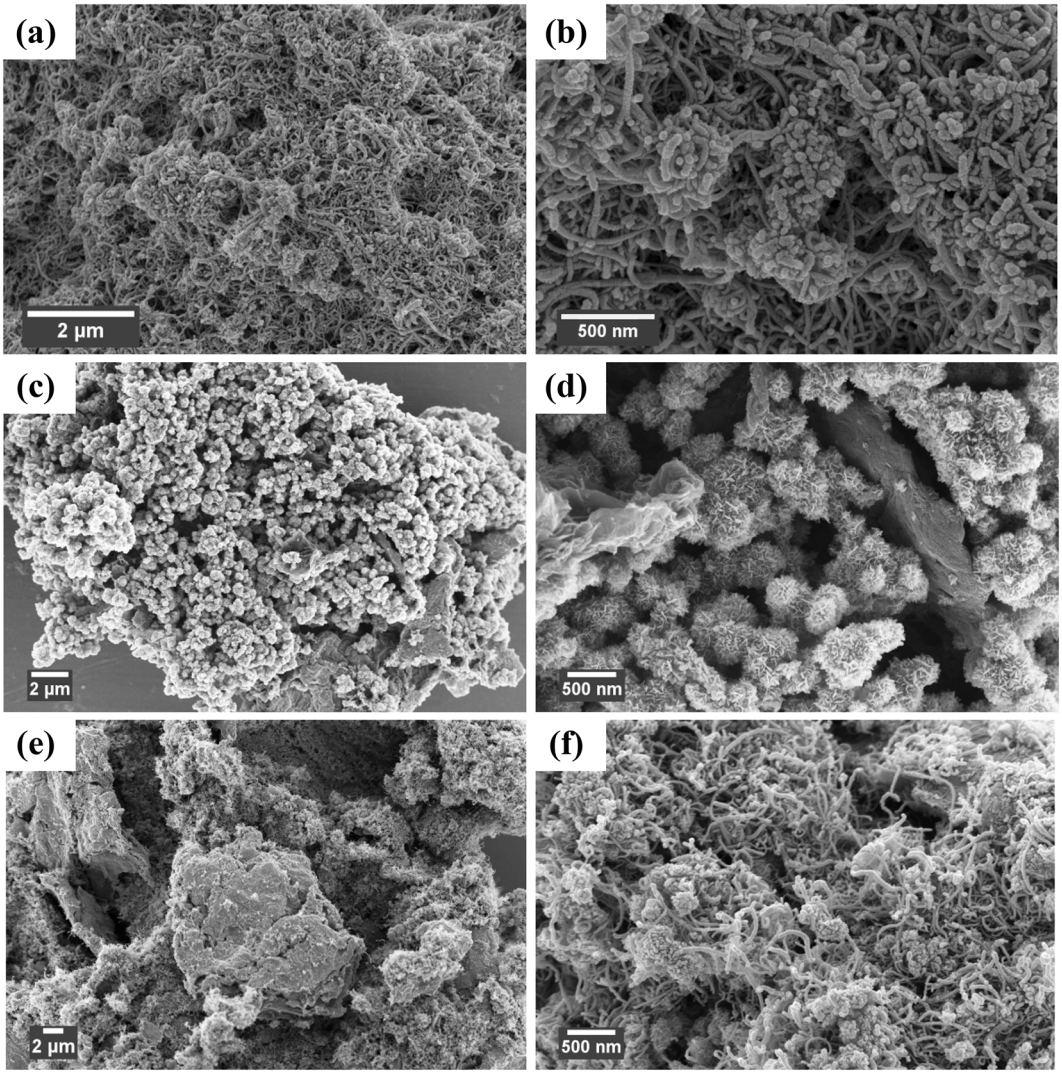

Fig. 3. FE-SEM images of (a-b) MnC, (c-d) MnG, and (e-f) MnGC nanocomposites in low and high resolution.

in the CV curves, which could be attributed to the oxygen–containing groups present in the MWCNTs and rGO. The CV curves of the MnC, MnG, and MnGC nanocomposites did not show much distortion and maintained a fairly rectangular shape even at higher scan rates (as shown in Fig. 6b-d). These results indicated that the nanocomposite electrodes possessed superior charge storage behavior with quick time response [44]. The pristine MWCNT and rGO electrodes displayed the influence of redox behavior along with double layer charge storage due to the presence of surface oxygen–containing groups. The CV curves of MWCNT, rGO exhibited excellent reversibility and negligible polarization at higher voltage scan rates (please refer to Fig. S8a, and c in Supplementary material). The larger area under the CV curves of the MnGC, MnC, and MnG, as compared to pristine rGO and MWCNT, indicated the increase in capacitance of nanocomposites due to the addition of MnO_2. These results indicated that the capacitance of the MnGC, MnC, and MnG electrodes was a combined contribution of double–layer capacitance of carbon components (MWCNTs and rGO) and pseudocapacitance from the MnO_2 and surface oxygen groups present in the carbon components. The charge storage of MnO_2 in both electrodes (due to their symmetric nature) could take place via either rapid adsorption of electrolyte cations (Na^+) on the surface (surface faradaic reaction) of the MnO_2 or intercalation/deintercalation of cations on in the bulk MnO_2 (bulk faradaic reaction).[45,46]

$$(MnO_2)_{surface} + Na^+ + e^- \leftrightarrow (MnOONa)_{surface} \quad (1)$$

$$MnO_2 + Na^+ + e^- \leftrightarrow MnOONa \quad (2)$$

The gravimetric capacitances of the SC electrodes at different scan rates were calculated (using equations described in Supplementary material) from CV curves and are presented in Fig. 6e. The MnGC nanocomposite electrodes demonstrated a high gravimetric capacitance of 314.6 F g^{-1} at 5 mV s^{-1} and this value is 1.34 × and 1.22 × higher than the capacitance of the MnC (235.1 F g^{-1}) and MnG (258.2 F g^{-1}) electrodes. Additionally, the capacitances of rGO and MWCNTs electrodes at 5 mV s^{-1} were calculated as 138.9 and 110.5 F g^{-1}, respectively. Notably, the specific capacitance obtained for the synthesized MnGC nanocomposites at commercial-level electrode mass loadings is superior to many earlier reports (please refer to Tables S2, and S3 in Supplementary material). Although some studies have reported astonishing capacitances for composites of graphene/CNTs with MnO_2, electrode mass loadings in these studies were very low ($\leq$1 – 2 mg cm^{-2}). Despite their extraordinary capacitances, the low mass loading electrodes cannot be used in commercial applications due to their poor actual capacity (as a result of the low ratio of active materials to a full cell). When the mass loading of the electrodes is increased, rapid fading of the capacitance is observed along with poor rate capability as evident in most of the studies [18,33]. As shown in Fig. 6e, the capacitances of

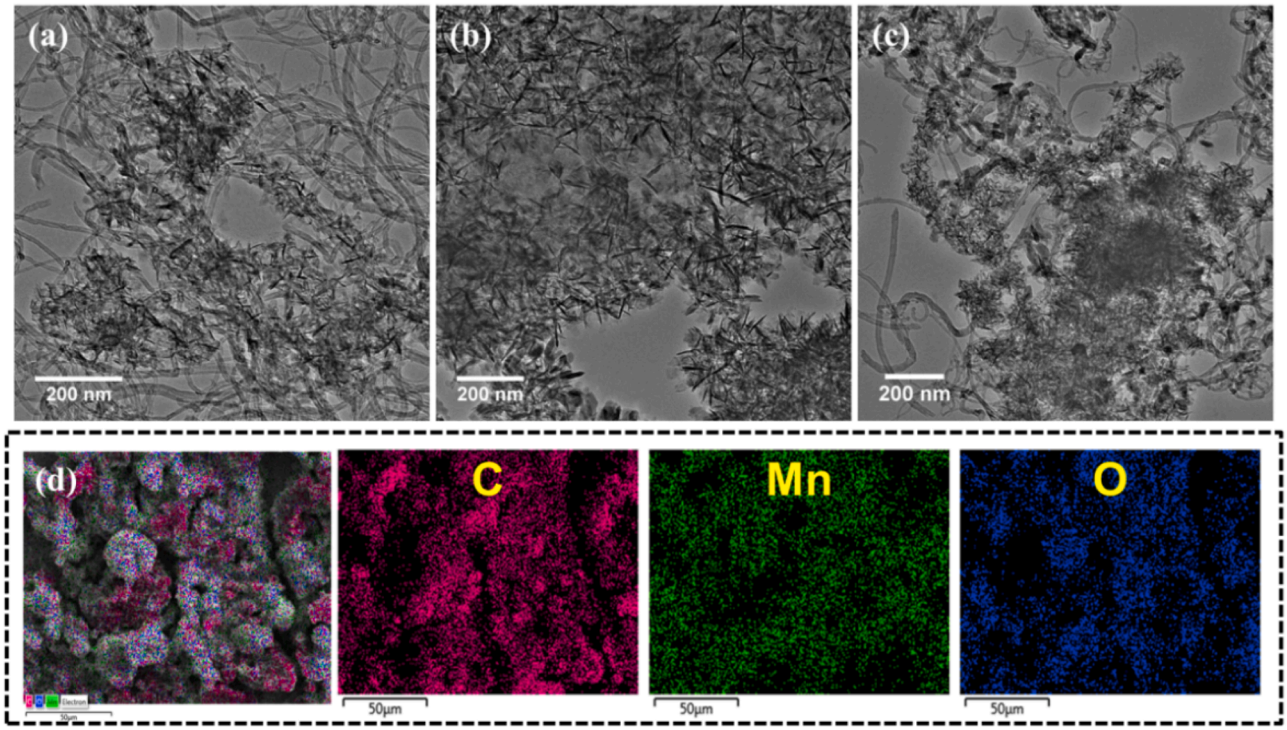

Fig. 4. TEM images of (a) MnC, (b) MnG, and (c) MnGC nanocomposites; (d) elemental mapping of MnGC nanocomposite (carbon in maroon, manganese in green, and oxygen in blue). (For interpretation of the references to colour in this figure legend, the reader is referred to the web version of this article.)

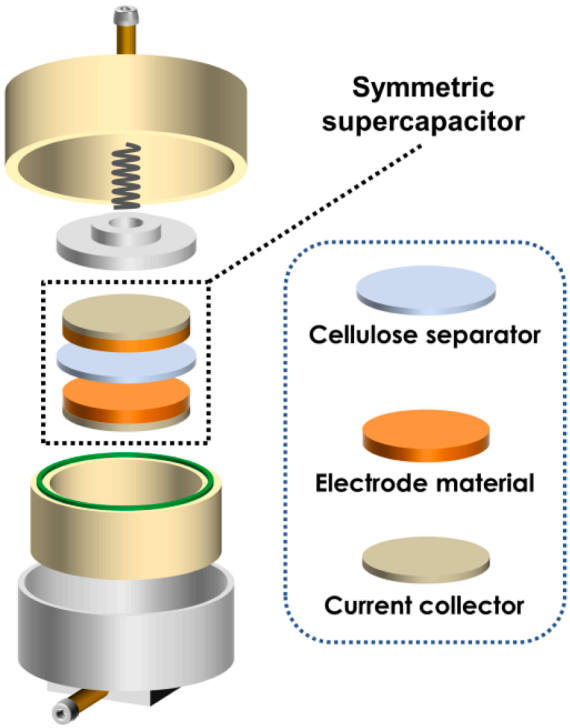

Fig. 5. Schematic of two-electrode symmetric SC cell and the split-type cell assembly.

the nanocomposite electrodes decreased at increased scan rates as the charge storage gets limited to the outer surface only at higher scan rates. The MnGC nanocomposite displayed a capacitance of 207 F g^{-1} at 50 mV s^{-1} and retained ~ 67 % of initial capacitance. Conversely, the MnC and MnG electrodes were able to retain 57.8 and 54.1 % of their capacitance when the scan rate was increased to 50 mV s^{-1}. Although the MnG electrodes exhibited superior capacitance as compared to MnC electrodes, the rate performance of the MnC electrodes was slightly better than the MnG. The relatively worse rate capability of MnG could be due to the dense aggregation of MnO_2 nanostructures on the surface of crumpled rGO resulting in sluggish ion transport dynamics. The relatively lower aggregation of MnO_2 on the MWCNTs surface has helped the MnC electrodes to retain comparatively better capacitance. Moreover, the superior rate capability of MnGC electrodes could be ascribed to the synergistic effect resulting from simultaneous growth of MnO_2 on the surfaces of both rGO and MWCNTs. The specific capacitances contributed by only MnO_2 (pseudocapacitance) in the nanocomposite electrodes were also calculated [5]. The capacitance of MnO_2 in the MnGC electrodes was 610.5 F g^{-1} at 5 mV s^{-1}, which was much higher compared to the MnC (442.8 F g^{-1}) and MnG (444.9 F g^{-1}) electrodes (shown in Fig. 6f).

It is noteworthy that the MnGC electrodes exhibited superior capacitive response compared to MnG electrodes despite its relatively lower specific surface area than MnG nanocomposite. This excellent capacitance of the MnGC could be ascribed to its unique microstructure that allowed maximum electrochemical utilization of the MnO_2 nanostructures and the reduction in diffusion length promoted faster charge transport. As a result, the MnO_2 nanostructures of MnGC effectively participated in the charge storage/delivery process exhibiting high pseudocapacitance, thereby enhancing the overall capacitance of the MnGC electrodes.

The electrochemical performance of the nanocomposite electrodes was further investigated by galvanostatic charge–discharge (GCD) at different current densities ranging from 0.2 to 5 A g^{-1}. The SC electrodes could work up to the potential of 1.5 V as observed in CV curves. The GCD curves of the SCs at 1 A g^{-1} are shown in Fig. 7a. The symmetric and linear GCD curves indicated the good capacitive behavior of the electrode materials [47]. Additionally, the absence of any voltage plateaus inferred that there is no bulk redox reaction during the charge–discharge process. The GCD curves of the SCs (shown in Fig. 7b-d, and Fig. S8b, d in Supplementary material) at varying current densities

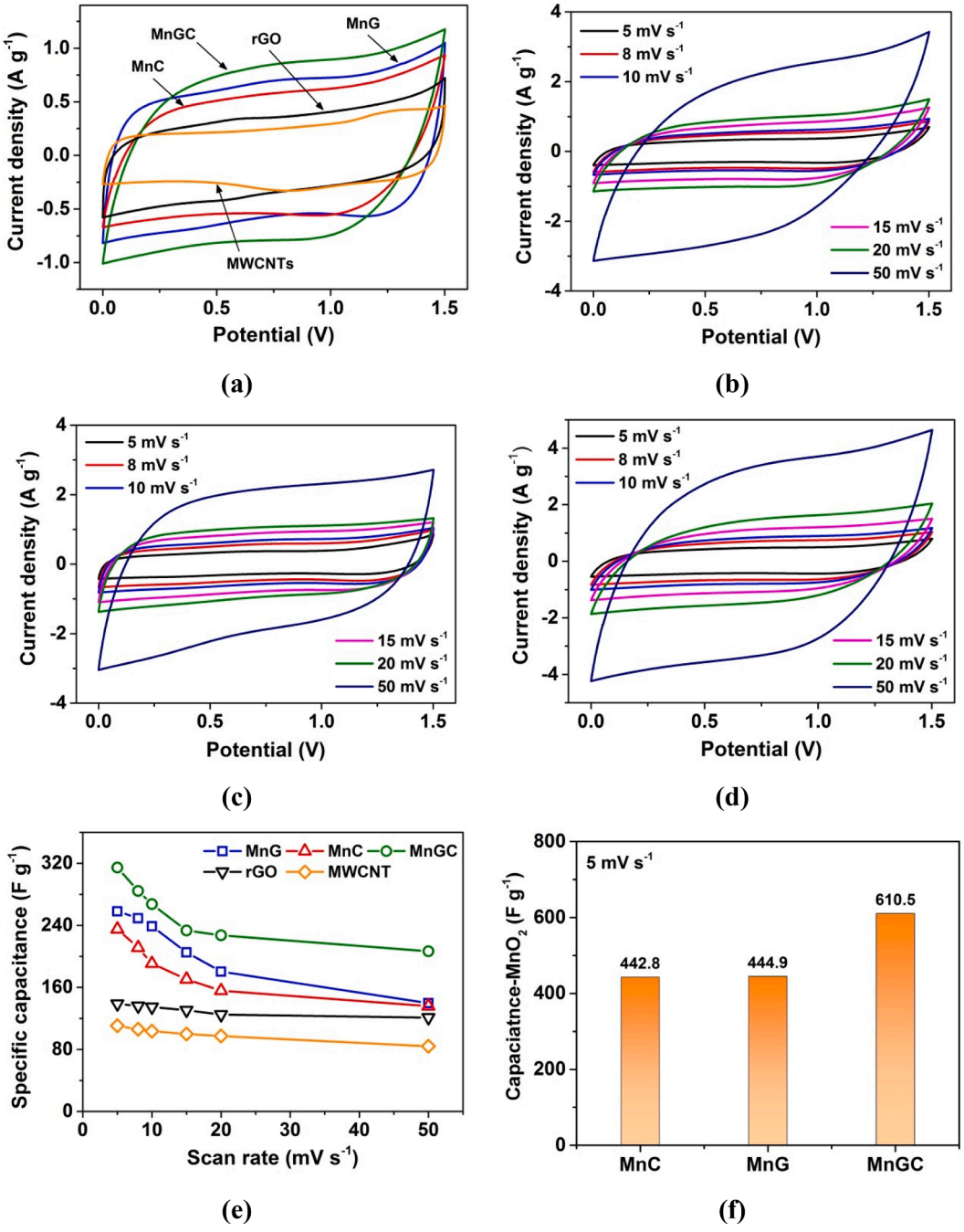

Fig. 6. (a) Comparison of CV curves of SCs at 10 mV s^{-1}; CV curves of (b) MnC, (c) MnG, and (d) MnGC SCs at various scan rates; (e) specific capacitance of the SC electrodes as a function of scan rate; (f) capacitance contribution of MnO_2 at 5 mV s^{-1}.

did not deviate from the symmetric and linear nature suggesting high reversibility of the charge storage process. The *IR* drop values were calculated from the GCD curves and found to be 0.09, 0.06, 0.09, 0.02, and 0.08 V for the MnC, MnG, MnGC, rGO, and MWCNT based SCs. The capacitances of the electrodes were evaluated from the GCD curves using as described in the Supplementary material. At a current density of 0.2 A g^{-1}, the capacitance of MnGC was calculated to be ~ 271.8 F g^{-1} which is 1.2×, 1.4×, 2.2×, 2.9 × the capacitance of the MnG (226.2 F g^{-1}), MnC (193.5 F g^{-1}), rGO (124.7 F g^{-1}), and MWCNT (94.5 F g^{-1}) electrodes, respectively. The decrease in capacitance of the electrodes for higher current density is evident from the smaller charge–discharge time of the GCD curves. This decreased capacitance could be ascribed to inadequate ion migration to the inner core of the electrodes and thereby impeding the charge transfer process [30]. Furthermore, the MnGC nanocomposites exhibited superior capacitance values as compared to the MnG and MnC even at high current densities (Fig. 7e). The MnGC electrode retained a capacitance of 194.6 F g^{-1} (71.5%) at 5 A g^{-1} demonstrating the superior rate capability as compared to the MnG (61.4%) and MnC (65.5%) electrodes. The unique structure of MnGC has efficient pore networks for rapid charge transfer, which results in its superior capacitance retention at high current densities.

The fabricated SCs were subjected to repetitive charge–discharge cycles at 5 A g^{-1} to study the electrochemical stability of the electrode materials. As shown in Fig. 7f, there was no prominent degradation in the capacitance for the MnGC and MnC SCs, demonstrating excellent electrochemical stability even after 5000 charge–discharge cycles. The capacitance of the MnGC SC increased to 103.4 % after 5000 cycles, as the electrode capacitance increased to 201.2 F g^{-1} from 194.6 F g^{-1}. The

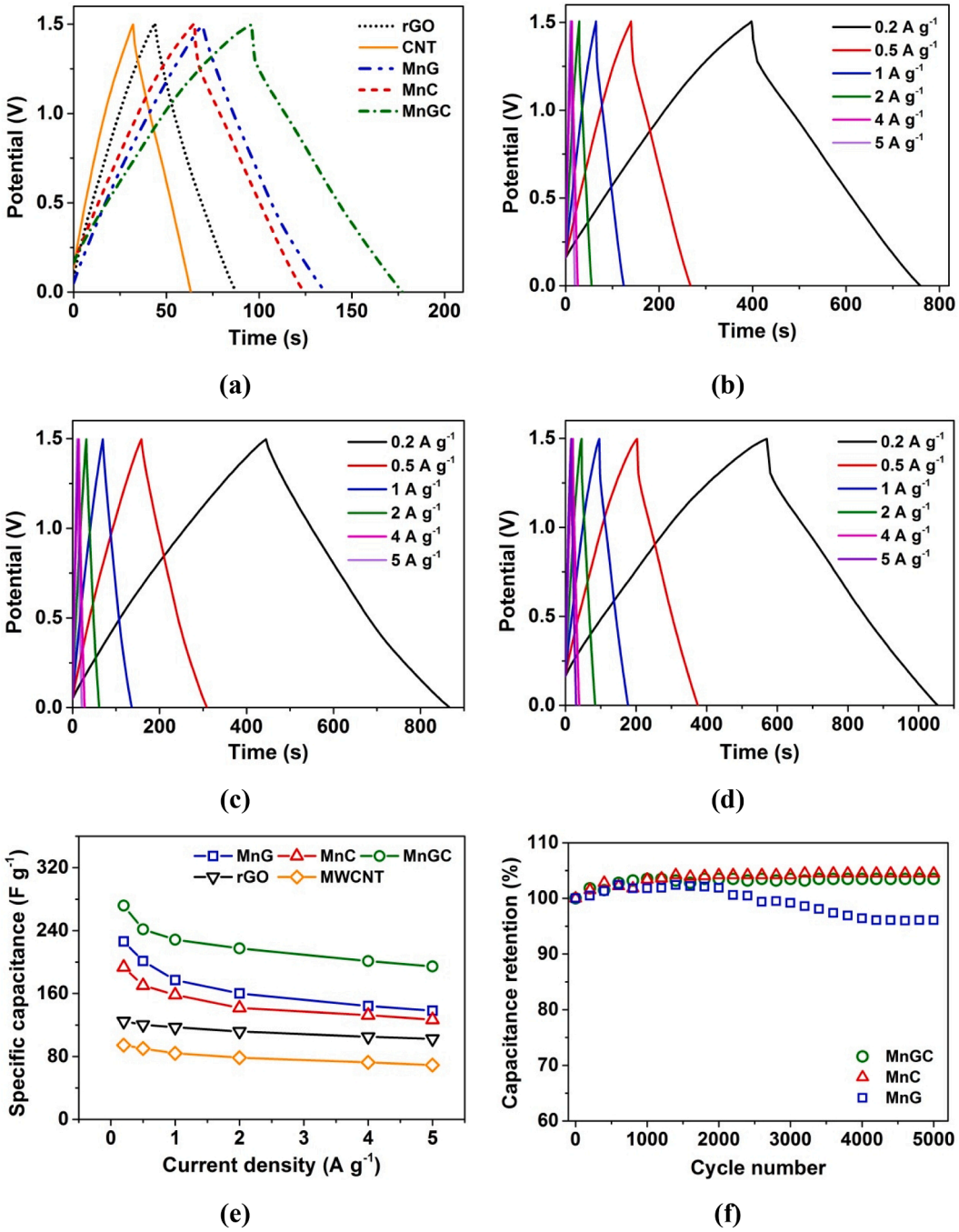

Fig. 7. (a) Comparison of GCD curves of SCs at 1 A g^{-1}; GCD curves of (b) MnC, (c) MnG, and (d) MnGC SCs at different current densities; (e) specific capacitance of the SC electrodes as a function of current density; (f) long-term cyclic stability of SC cells.

MnC SC demonstrated 104.5% of initial capacitance after charge–discharge tests. Conversely, MnG SC was able to retain about 96.1% of its initial capacitance. Plausibly the electrolytes ions could not utilize the maximum available electrochemical area of the thicker (due to high mass loading) electrodes at the initial charge–discharge cycles. When the SCs were cycled for a few hundred cycles, the electrolyte ions were able to penetrate deeper into the pore structure as a result of the continuous charge–discharge process (and application of voltage). Thus the electrochemically active area for charge storage must have increased and as a result, the capacitances of the electrodes were gradually increased up to ~ 1000 cycles. The MnGC and MnC SCs were able to retain the increased capacitance whereas the MnG SC suffered a 3.9% loss in capacitance after 5000 charge–discharge cycles. This loss of capacitance could be due to poor capacitance retention of densely grown MnO_2 in the MnG nanocomposite [48]. Furthermore, excellent capacitance retention was exhibited by the pristine rGO and MWCNT SCs, maintaining approximately 100% of its initial capacitance after cycle tests (refer to Fig. S9a in Supplementary material). The capacitive performance of the MnGC nanocomposites was compared with the existing reports of MnO_2–carbon based composites and found to be superior to many studies despite high electrode mass loading of 12 mg cm^{-2} (please refer to Tables S2, and S3 in Supplementary material).

The electrochemical impedance data of the SCs was recorded using a sinusoidal signal of 10 mV s^{-1} in the frequency range of 10^5 – 0.01 Hz. The Nyquist plots of MnGC, MnC, and MnG SCs are shown in Fig. 8a. The points in Fig. 8a represent the impedance data recorded before cycle

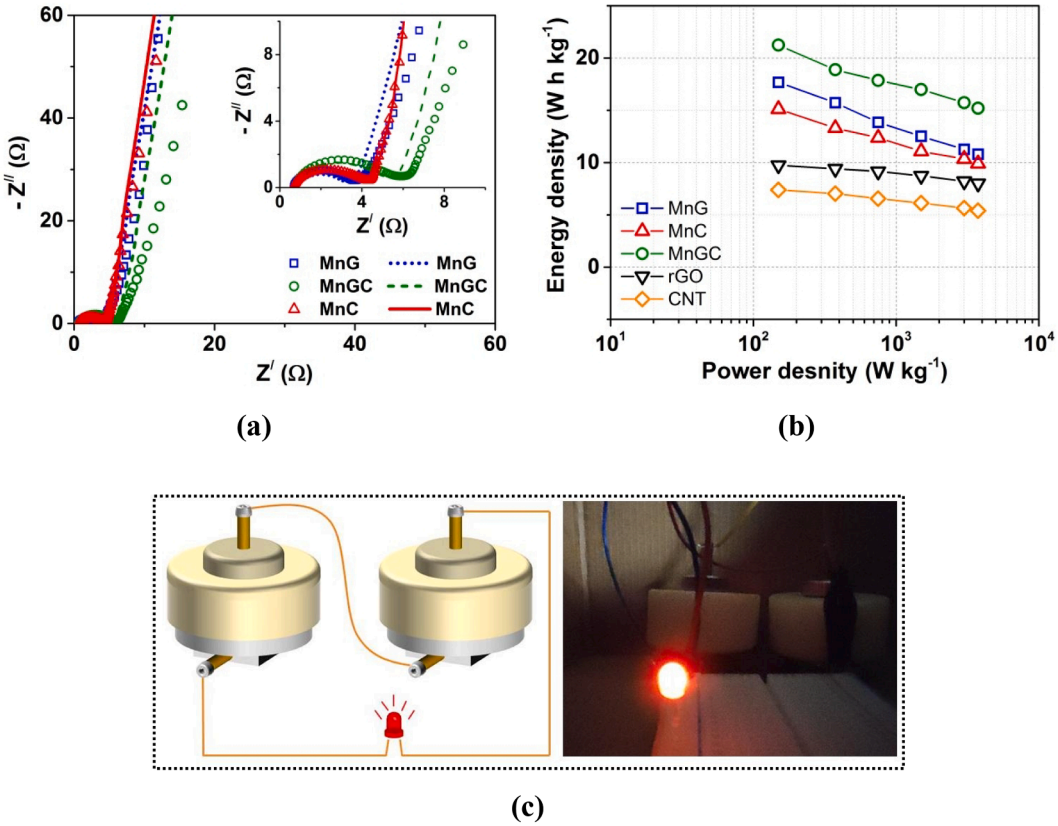

Fig. 8. (a) Nyquist plots (lines – EIS data recorded after 5000 cycles) and (b) Ragone plot of MnC, MnG, and MnGC SCs; (c) schematic diagram and photo of the red LED powered by two MnGC SCs connected in series. (For interpretation of the references to colour in this figure legend, the reader is referred to the web version of this article.)

stability tests, whereas the lines denote impedance data recorded after cycle stability tests, i.e. after 5000 charge–discharge cycles. In the high–frequency region, the impedance spectra of the SCs form a semi–circular arc and a straight line in the low–frequency region [49]. The intercept in the real Z' axis at very high frequency denotes a series resistance (R_s), which originates from the combined effect of electrolyte resistance, and other intrinsic resistances of the system [5]. The semi–circle of the Nyquist plot accounts for the charge transfer resistance (R_{ct}) associated with the charge transfer via double layer formation and faradaic redox reactions at the electrode/electrolyte interface [50,51]. The equivalent circuit for the impedance data is shown in Fig. S9b (inset) in Supplementary material. Before cycle stability tests, the R_s values for the MnC, MnG, and MnGC SCs were in the range of ~ 0.67–0.7 Ω, indicating high ionic conductivity and low resistance in the system. After the charge–discharge cycles, the measured R_s values were 0.83, 0.87, and 0.69 Ω, respectively for MnC, MnG, and MnGC. The charge transfer resistances were calculated from the semicircular arc and the MnG sample showed the least charge transfer resistance with an initial R_{ct} value of 2.92 Ω as compared to MnC (3.45 Ω), and MnGC (4.87 Ω). After being subjected to charge–discharge cycles, the charge transfer resistance was reduced to 3.31, 2.32, and 4.39 Ω, respectively for MnC, MnG, and MnGC SCs. Reduction in R_{ct} values indicted the improved charge transport in the electrodes during charge–discharge tests. In the high–frequency region, the impedance spectra of all the three SCs showed vertical lines, exhibiting ideal supercapacitive behavior. These lines became more vertical after cycle stability tests, which indicated smaller diffusion resistance as a result of faster ion transfer dynamics after repetitive charge–discharge cycles. A similar observation of reduced charge transfer resistance after cycle stability tests was also noticeable in the Nyquist plots of the rGO and MWCNT SCs, as shown in Fig. S9b (in Supplementary material). The reduction in charge transfer and diffusion resistance value supports the observation that the capacitances of the SCs increased after the initial ~ 1000 charge–discharge cycles. The electrochemical performance of the MnO_2 based SC is illustrated in Fig. S10 (Supplementary material). The electrochemical data in Fig. S10 (please refer to Supplementary material) indicated sluggish charge transport, poor rate capability of the high mass loading MnO_2 electrodes.

The performances of the fabricated SCs were also compared based on energy and power densities. The Ragone plots of the MnC, MnG, MnGC, MWCNT, and rGO based SC cells are given in Fig. 8b. The energy density of the MnGC SC was calculated to be 21.2 W h kg^{-1} (at a power density of 150 W kg^{-1}), and this value is 1.4×, 1.2×, 2.9×, and 2.2 × higher than the energy densities of MnC (15.12 W h kg^{-1}), MnG (17.67 W h kg^{-1}), MWCNT (7.38 W h kg^{-1}), and rGO (9.74 W h kg^{-1}) SCs, respectively. The MnGC SC was able to maintain its superior energy density as compared to the MnG and MnC SCs even at higher power densities and delivered an energy density of 15.2 W h kg^{-1} at 3750 W kg^{-1}. The high energy density of the nanocomposite SCs could be ascribed to the improved capacitance of nanocomposites with high pseudocapacitive contribution from MnO_2. Additionally, the energy density of the MnGC SC is superior to many MnO_2/carbon-based SCs reported elsewhere [27,52-55]. Fig. 8c depicts the schematic and photo of two MnGC SCs in series, which could power a red LED for a few minutes.

3.3. Physical explanation for the influence of ultrasound

The ultrasonic irradiation during synthesis creates intense micro-convection in the system. Propagation of ultrasound waves induces high-frequency oscillations of fluid elements at a very small spatial scale. The amplitude of oscillation (a) of fluid elements in our system was

calculated to be $a = 0.43$ μm [36]. As a result of this intense micro-convection at a very small spatial scale, the rGO is efficiently exfoliated and MWCNTs could be uniformly intercalated as spacers to prevent restacking of rGO sheets that facilitate easier diffusion of ions. Additionally, sonication lowers the aggregation of MnO_2 nanostructure and promotes simultaneous growth of MnO_2 on rGO and MWCNTs resulting in the formation of the ternary MnGC nanocomposite. The superior electrochemical performance displayed by the MnGC nanocomposite could be attributed to its porous microstructure. The self–assembly of the MnO_2 nanostructures on the surface of rGO and MWCNTs reduced aggregation and created abundant pores resulting in improved diffusion of electrolyte ions (i.e. Na^+) inside the whole composite electrode. Moreover, the addition of MWCNTs to rGO increased the electrochemically active surface area of the MnGC nanocomposite as well as the MnO_2 nanostructures. As a result, the diffusion length for the electrolyte ions gets reduced and more electrolyte ions could participate in charge storage and this was reflected in the superior rate capability of the MnGC electrodes. The carbon components in the nanocomposites (i.e. rGO and MWCNTs) act as conductive substrates for MnO_2 growth that provide excellent interfacial contact and facilitate easier electron transfer in the whole electrode. This interfacial synergism between individual components of the MnGC nanocomposite, in conjunction with the morphological features contributing to rapid charge transport, results in its excellent electrochemical performance.

4. Conclusions

In summary, a ternary nanocomposite of MWCNT/MnO_2/rGO (MnGC) was synthesized via a novel one–pot ultrasound–assisted method. The synthesized MnGC nanocomposite possessed a mesoporous structure with a high BET surface area of ~ 313.2 $m^2\,g^{-1}$. The abundant pores present in the MnGC nanocomposite facilitated better electrolyte diffusion, maximum utilization of active surface area of MnO_2, reduced diffusion length, and rapid electron transport via its conductive network. As a whole, the synergistic interaction of all the individual components enhanced the energy storage capacity of MnGC electrodes. The symmetric SC fabricated with commercial-level mass loading MnGC electrodes, demonstrated notable enhancement in the capacitive behavior compared to binary nanocomposite (i.e. MnO_2/MWCNT and MnO_2/rGO) based SCs. The MnGC based SC displayed a wide operating voltage of 1.5 V in Na_2SO_4 electrolyte and a high gravimetric capacitance of 314.6 F g^{-1} (at 5 mV s^{-1}) was obtained for the MnGC electrodes. Moreover, the SC displayed excellent cycle stability with ~ 103.4 % capacitance retention after 5000 cycles at 5 A g^{-1}. The MnGC based SC delivered energy density as high as 21.2 W h kg^{-1} at a power density of 150 W kg^{-1}, which was 1.4×, 1.2×, 2.9×, and 2.2 × higher than the energy density of MnO_2/MWCNT, MnO_2/rGO, MWCNT, and rGO based symmetric SCs, respectively. The results of the present study clearly show the potential of ternary MnGC nanocomposite-based aqueous supercapacitors for applications in commercial scale energy storage systems.

CRediT authorship contribution statement

Bhaskar J. Choudhury: Conceptualization, Methodology, Investigation, Formal analysis, Validation, Writing – original draft. **Vijayanand S. Moholkar:** Conceptualization, Supervision, Project administration, Writing – review & editing.

Declaration of Competing Interest

The authors declare that they have no known competing financial interests or personal relationships that could have appeared to influence the work reported in this paper.

Acknowledgment

The authors would like to acknowledge the analytical facilities provided by the Central Instruments Facility (CIF) of Indian Institute of Technology Guwahati.

Appendix A. Supplementary data

Supplementary data to this article can be found online at https://doi.org/10.1016/j.ultsonch.2021.105896.

References

[1] P. Simon, Y. Gogotsi, Materials for electrochemical capacitors, Nat. Mater. 7 (11) (2008) 845–854.
[2] L. Zhang, X.S. Zhao, Carbon-based materials as supercapacitor electrodes, Chem. Soc. Rev. 38 (2009) 2520–2531, https://doi.org/10.1039/b813846j.
[3] S. Alireza Hashemi, S. Mojtaba Mousavi, H. Reza Naderi, S. Bahrani, M. Arjmand, A. Hagfeldt, W.-H. Chiang, S. Ramakrishna, Reinforced polypyrrole with 2D graphene flakes decorated with interconnected nickel-tungsten metal oxide complex toward superiorly stable supercapacitor, Chem. Eng. J. 418 (2021) 129396, https://doi.org/10.1016/j.cej.2021.129396.
[4] A. González, E. Goikolea, J.A. Barrena, R. Mysyk, Review on supercapacitors: Technologies and materials, Renew. Sustain. Energy Rev. 58 (2016) 1189–1206, https://doi.org/10.1016/j.rser.2015.12.249.
[5] J. Zhi, O. Reiser, F. Huang, Hierarchical MnO2 Spheres Decorated by Carbon-Coated Cobalt Nanobeads: Low-Cost and High-Performance Electrode Materials for Supercapacitors, ACS Appl. Mater. Interfaces 8 (13) (2016) 8452–8459.
[6] B. Gnana Sundara Raj, A.M. Asiri, A.H. Qusti, J.J. Wu, S. Anandan, Sonochemically synthesized MnO2 nanoparticles as electrode material for supercapacitors, Ultrason. Sonochem. 21 (6) (2014) 1933–1938.
[7] S. Ghasemi, S.R. Hosseini, O. Boore-talari, Sonochemical assisted synthesis MnO2/RGO nanohybrid as effective electrode material for supercapacitor, Ultrason. Sonochem. 40 (2018) 675–685, https://doi.org/10.1016/J.ULTSONCH.2017.08.013.
[8] P. Gao, P. Metz, T. Hey, Y. Gong, D. Liu, D.D. Edwards, J.Y. Howe, R. Huang, S. T. Misture, The critical role of point defects in improving the specific capacitance of δ-MnO2 nanosheets, Nat. Commun. 81 (8) (2017) 1–10, https://doi.org/10.1038/ncomms14559.
[9] Y.-H. Liu, H.-C. Hsi, K.-C. Li, C.-H. Hou, Electrodeposited Manganese Dioxide/Activated Carbon Composite As a High-Performance Electrode Material for Capacitive Deionization, ACS Sustain. Chem. Eng. 4 (9) (2016) 4762–4770.
[10] Y. Wang, H. Guan, S. Du, Y. Wang, A facile hydrothermal synthesis of MnO2 nanorod–reduced graphene oxide nanocomposites possessing excellent microwave absorption properties, RSC Adv. 5 (108) (2015) 88979–88988, https://doi.org/10.1039/C5RA15165A.
[11] J. Yao, Q. Pan, S. Yao, L. Duan, J. Liu, Mesoporous MnO2 Nanosphere/Graphene Sheets as Electrodes for Supercapacitor Synthesized by a Simple and Inexpensive Reflux Reaction, Electrochim. Acta 238 (2017) 30–35, https://doi.org/10.1016/J.ELECTACTA.2017.02.153.
[12] R. Liu, J. Duay, S.B. Lee, Electrochemical Formation Mechanism for the Controlled Synthesis of Heterogeneous MnO2/Poly(3,4-ethylenedioxythiophene) Nanowires, ACS Nano 5 (7) (2011) 5608–5619.
[13] J.W. Wang, Y. Chen, B.Z. Chen, Synthesis and control of high-performance MnO2/carbon nanotubes nanocomposites for supercapacitors, J. Alloy. Compd. 688 (2016) 184–197, https://doi.org/10.1016/J.JALLCOM.2016.07.005.
[14] J. Wang, X. Guo, R. Cui, H. Huang, B. Liu, Y. Li, D. Wang, D. Zhao, J. Dong, S. Li, B. Sun, MnO2/Porous Carbon Nanotube/MnO2 Nanocomposites for High-Performance Supercapacitor, ACS Appl. Nano Mater. 3 (11) (2020) 11152–11159.
[15] J. Li, M. Östling, Prevention of Graphene Restacking for Performance Boost of Supercapacitors—A Review, Crystals 3 (1) (2013) 163–190, https://doi.org/10.3390/cryst3010163.
[16] Y. Zhou, X.C. Hu, S. Guo, C. Yu, S. Zhong, X. Liu, Multi-functional graphene/carbon nanotube aerogels for its applications in supercapacitor and direct methanol fuel cell, Electrochim. Acta 264 (2018) 12–19, https://doi.org/10.1016/J.ELECTACTA.2018.01.009.
[17] S.-Y. Yang, K.-H. Chang, H.-W. Tien, Y.-F. Lee, S.-M. Li, Y.-S. Wang, J.-Y. Wang, C.-C. Ma, C.-C. Hu, Design and tailoring of a hierarchical graphene-carbon nanotube architecture for supercapacitors, J. Mater. Chem. 21 (7) (2011) 2374–2380, https://doi.org/10.1039/C0JM03199B.
[18] Y. Wang, W. Lai, N.i. Wang, Z. Jiang, X. Wang, P. Zou, Z. Lin, H.J. Fan, F. Kang, C.-P. Wong, C. Yang, A reduced graphene oxide/mixed-valence manganese oxide composite electrode for tailorable and surface mountable supercapacitors with high capacitance and super-long life, Energy Environ. Sci. 10 (4) (2017) 941–949, https://doi.org/10.1039/C6EE03773A.
[19] H. Xia, Y. Wang, J. Lin, L. Lu, Hydrothermal synthesis of MnO2/CNT nanocomposite with a CNT core/porous MnO2 sheath hierarchy architecture for supercapacitors, Nanoscale Res. Lett. 71 (7) (2012) 1–10, https://doi.org/10.1186/1556-276X-7-33.
[20] Y.u. Jin, H. Chen, M. Chen, N. Liu, Q. Li, Graphene-Patched CNT/MnO2 Nanocomposite Papers for the Electrode of High-Performance Flexible Asymmetric Supercapacitors, ACS Appl. Mater. Interfaces 5 (8) (2013) 3408–3416.

[21] B. Wei, L. Wang, Q. Miao, Y. Yuan, P. Dong, R. Vajtai, W. Fei, Fabrication of manganese oxide/three-dimensional reduced graphene oxide composites as the supercapacitors by a reverse microemulsion method, Carbon N. Y. 85 (2015) 249–260, https://doi.org/10.1016/J.CARBON.2014.12.063.
[22] B. Unnikrishnan, C.-W. Wu, I.-W. Chen, H.-T. Chang, C.-H. Lin, C.-C. Huang, Carbon Dot-Mediated Synthesis of Manganese Oxide Decorated Graphene Nanosheets for Supercapacitor Application, ACS Sustain. Chem. Eng. 4 (6) (2016) 3008–3016.
[23] Y. Liu, X. Miao, J. Fang, X. Zhang, S. Chen, W. Li, W. Feng, Y. Chen, W. Wang, Y. Zhang, Layered-MnO2 Nanosheet Grown on Nitrogen-Doped Graphene Template as a Composite Cathode for Flexible Solid-State Asymmetric Supercapacitor, ACS Appl. Mater. Interfaces 8 (8) (2016) 5251–5260.
[24] B. Yao, S. Chandrasekaran, J. Zhang, W. Xiao, F. Qian, C. Zhu, E.B. Duoss, C. M. Spadaccini, M.A. Worsley, Y. Li, Efficient 3D Printed Pseudocapacitive Electrodes with Ultrahigh MnO2 Loading, Joule. 3 (2) (2019) 459–470.
[25] L. Hu, W. Chen, X. Xie, N. Liu, Y. Yang, H. Wu, Y. Yao, M. Pasta, H.N. Alshareef, Y. i. Cui, Symmetrical MnO2–Carbon Nanotube-Textile Nanostructures for Wearable Pseudocapacitors with High Mass Loading, ACS Nano 5 (11) (2011) 8904–8913.
[26] Z. Lei, F. Shi, L.i. Lu, Incorporation of MnO2-Coated Carbon Nanotubes between Graphene Sheets as Supercapacitor Electrode, ACS Appl. Mater. Interfaces 4 (2) (2012) 1058–1064.
[27] Y. Cheng, S. Lu, H. Zhang, C.V. Varanasi, J. Liu, Synergistic Effects from Graphene and Carbon Nanotubes Enable Flexible and Robust Electrodes for High-Performance Supercapacitors, Nano Lett. 12 (8) (2012) 4206–4211.
[28] G. Zhu, Z. He, J. Chen, J. Zhao, X. Feng, Y. Ma, Q. Fan, L. Wang, W. Huang, Highly conductive three-dimensional MnO2–carbon nanotube–graphene–Ni hybrid foam as a binder-free supercapacitor electrode, Nanoscale. 6 (2) (2014) 1079–1085, https://doi.org/10.1039/C3NR04495E.
[29] H. Jiang, Y. Dai, Y. Hu, W. Chen, C. Li, Nanostructured Ternary Nanocomposite of rGO/CNTs/MnO2 for High-Rate Supercapacitors, ACS Sustain. Chem. Eng. 2 (1) (2014) 70–74.
[30] R. Wu, D.P. Wang, V. Kumar, K. Zhou, A.W.K. Law, P.S. Lee, J. Lou, Z. Chen, MOFs-derived copper sulfides embedded within porous carbon octahedra for electrochemical capacitor applications, Chem. Commun. 51 (15) (2015) 3109–3112.
[31] Y. Zhang, X. Cui, J. Fu, Y. Liu, Y. Wu, J. Zhou, Z. Zhang, E. Xie, Commercial-level mass-loading MnO2 with ion diffusion channels for high-performance aqueous energy storage devices, J. Mater. Chem. A 9 (33) (2021) 17945–17954, https://doi.org/10.1039/D1TA04850C.
[32] Y. Dong, J. Zhu, Q. Li, S.u. Zhang, H. Song, D. Jia, Carbon materials for high mass-loading supercapacitors: filling the gap between new materials and practical applications, J. Mater. Chem. A 8 (42) (2020) 21930–21946, https://doi.org/10.1039/D0TA08265A.
[33] W. Guo, C. Yu, S. Li, J. Qiu, Toward commercial-level mass-loading electrodes for supercapacitors: opportunities, challenges and perspectives, Energy Environ. Sci. 14 (2) (2021) 576–601, https://doi.org/10.1039/D0EE02649B.
[34] W. Zheng, J. Halim, Z.M. Sun, J. Rosen, M.W. Barsoum, MXene—manganese oxides aqueous asymmetric supercapacitors with high mass loadings, high cell voltages and slow self-discharge, Energy Storage Mater. 38 (2021) 438–446, https://doi.org/10.1016/J.ENSM.2021.03.011.
[35] R.i. Chen, M. Yu, R.P. Sahu, I.K. Puri, I. Zhitomirsky, The Development of Pseudocapacitor Electrodes and Devices with High Active Mass Loading, Adv. Energy Mater. 10 (20) (2020) 1903848, https://doi.org/10.1002/aenm.v10.2010.1002/aenm.201903848.
[36] B.J. Choudhury, K. Roy, V.S. Moholkar, Improvement of Supercapacitor Performance through Enhanced Interfacial Interactions Induced by Sonication, Ind. Eng. Chem. Res. 60 (20) (2021) 7611–7623.
[37] S. Devaraj, N. Munichandraiah, Effect of Crystallographic Structure of MnO2 on Its Electrochemical Capacitance Properties, J. Phys. Chem. C 112 (11) (2008) 4406–4417.
[38] H.U. Shah, F. Wang, M.S. Javed, M.A. Ahmad, M. Saleem, J. Zhan, Z.U.H. Khan, Y. Li, In-situ growth of MnO2 nanorods forest on carbon textile as efficient electrode material for supercapacitors, J. Energy Storage. 17 (2018) 318–326, https://doi.org/10.1016/J.EST.2018.03.015.
[39] J. Xu, S. Gai, F. He, N.a. Niu, P. Gao, Y. Chen, P. Yang, A sandwich-type three-dimensional layered double hydroxide nanosheet array/graphene composite: fabrication and high supercapacitor performance, J. Mater. Chem. A 2 (4) (2014) 1022–1031, https://doi.org/10.1039/C3TA14048B.
[40] L. Li, R. Li, S. Gai, P. Gao, F. He, M. Zhang, Y. Chen, P. Yang, Hierarchical porous CNTs@NCS@MnO 2 composites: rational design and high asymmetric supercapacitor performance, J. Mater. Chem. A 3 (30) (2015) 15642–15649, https://doi.org/10.1039/C5TA03224E.
[41] C. Zhong, Y. Deng, W. Hu, J. Qiao, L. Zhang, J. Zhang, A review of electrolyte materials and compositions for electrochemical supercapacitors, Chem. Soc. Rev. 44 (21) (2015) 7484–7539, https://doi.org/10.1039/C5CS00303B.
[42] X. Zhao, L. Zhang, S. Murali, M.D. Stoller, Q. Zhang, Y. Zhu, R.S. Ruoff, Incorporation of manganese dioxide within ultraporous activated graphene for high-performance electrochemical capacitors, ACS Nano 6 (6) (2012) 5404–5412, https://doi.org/10.1021/nn3012916.
[43] J. Yan, J. Liu, Z. Fan, T. Wei, L. Zhang, High-performance supercapacitor electrodes based on highly corrugated graphene sheets, Carbon N. Y. 50 (6) (2012) 2179–2188, https://doi.org/10.1016/j.carbon.2012.01.028.
[44] J. Chen, K. Fang, Q. Chen, J. Xu, C.P. Wong, Integrated paper electrodes derived from cotton stalks for high-performance flexible supercapacitors, Nano Energy 53 (2018) 337–344, https://doi.org/10.1016/j.nanoen.2018.08.056.
[45] J. Zhu, W. Shi, N.i. Xiao, X. Rui, H. Tan, X. Lu, H.H. Hng, J. Ma, Q. Yan, Oxidation-Etching Preparation of MnO2 Tubular Nanostructures for High-Performance Supercapacitors, ACS Appl. Mater. Interfaces 4 (5) (2012) 2769–2774.
[46] Q.-Z. Zhang, D. Zhang, Z.-C. Miao, X.-L. Zhang, S.-L. Chou, Research Progress in MnO2–Carbon Based Supercapacitor Electrode Materials, Small 14 (24) (2018) 1702883, https://doi.org/10.1002/smll.v14.2410.1002/smll.201702883.
[47] G. Yu, L. Hu, N. Liu, H. Wang, M. Vosgueritchian, Y. Yang, Y.i. Cui, Z. Bao, Enhancing the supercapacitor performance of graphene/MnO2 nanostructured electrodes by conductive wrapping, Nano Lett. 11 (10) (2011) 4438–4442, https://doi.org/10.1021/nl2026635.
[48] S. Zhu, L. Fan, Y. Lu, Highly uniform Fe3O4 nanoparticle-rGO composites as anode materials for high performance lithium-ion batteries, RSC Adv. 7 (87) (2017) 54939–54946.
[49] Z. Ping, L. XiaoJing, R. Anye, G. Peng, Preparation of a novel porous gel electrolyte and its application in micro supercapacitor, J. Electroanal. Chem. 782 (2016) 154–160, https://doi.org/10.1016/J.JELECHEM.2016.10.021.
[50] J. Zhi, W. Zhao, X. Liu, A. Chen, Z. Liu, F. Huang, Highly conductive ordered mesoporous carbon based electrodes decorated by 3D graphene and 1D silver nanowire for flexible supercapacitor, Adv. Funct. Mater. 24 (14) (2014) 2013–2019, https://doi.org/10.1002/adfm.201303082.
[51] J. Zhi, S. Deng, Y. Wang, A. Hu, Highly ordered metal oxide nanorods inside mesoporous silica supported carbon nanomembranes: High performance electrode materials for symmetrical supercapacitor devices, J. Phys. Chem. C 119 (16) (2015) 8530–8536, https://doi.org/10.1021/acs.jpcc.5b01230.
[52] E. Miniach, A. Śliwak, A. Moyseowicz, L. Fernández-Garcia, Z. González, M. Granda, R. Menendez, G. Gryglewicz, MnO2/thermally reduced graphene oxide composites for high-voltage asymmetric supercapacitors, Electrochim. Acta 240 (2017) 53–62, https://doi.org/10.1016/J.ELECTACTA.2017.04.056.
[53] Y. Liu, D. He, H. Wu, J. Duan, Y. Zhang, Hydrothermal Self-assembly of Manganese Dioxide/Manganese Carbonate/Reduced Graphene Oxide Aerogel for Asymmetric Supercapacitors, Electrochim. Acta 164 (2015) 154–162, https://doi.org/10.1016/J.ELECTACTA.2015.01.223.
[54] D.G. Lee, Y.A. Kim, B.H. Kim, Capacitive properties of hierarchically structured carbon nanofiber/graphene/MnO2 hybrid electrode with nitrogen and oxygen heteroatoms, Carbon N. Y. 107 (2016) 783–791, https://doi.org/10.1016/J.CARBON.2016.06.093.
[55] L. Deng, G. Zhu, J. Wang, L. Kang, Z.-H. Liu, Z. Yang, Z. Wang, Graphene–MnO2 and graphene asymmetrical electrochemical capacitor with a high energy density in aqueous electrolyte, J. Power Sources 196 (24) (2011) 10782–10787.